

PAPER

# Estimation of microtexture region orientation distribution functions using eddy current data

To cite this article: Laura Homa *et al* 2021 *Inverse Problems* **37** 065004

View the [article online](#) for updates and enhancements.

## You may also like

- [Multifractal Analysis of Pulsar Timing Residuals: Assessment of Gravitational Wave Detection](#)  
I. Eghdami, H. Panahi and S. M. S. Movahed
- [Microtextured die using silicon stencil mask for micro-machining of stainless steel](#)  
Gang Han and Minoru Sasaki
- [Microtexture diagnostics of asphalt pavement surfaces](#)  
Zuzana Florková and L'ubomír Pepucha

# Estimation of microtexture region orientation distribution functions using eddy current data

Laura Homa<sup>1,\*</sup> , Matthew Cherry<sup>2</sup> and John Wertz<sup>2</sup>

<sup>1</sup> University of Dayton Research Institute, Dayton, OH, 45469, United States of America

<sup>2</sup> Air Force Research Laboratory, WPAFB, OH, 45433, United States of America

E-mail: [laura.homa@udri.udayton.edu](mailto:laura.homa@udri.udayton.edu)

Received 20 October 2020, revised 20 April 2021

Accepted for publication 26 April 2021

Published 7 June 2021



## Abstract

Microtexture regions (MTRs) within titanium alloys are collections of grains with similar crystallographic orientation. The presence of MTRs can be detrimental to the life of an engine component; as such, a method to detect and characterize MTRs is needed. One potential technique to characterize MTRs is eddy current (EC) testing, which is a nondestructive evaluation technique that is sensitive to the changes in local conductivity due to changes in local crystallographic orientation. While it has been established in the literature that EC methods are sensitive to the presence of MTRs, work has begun only recently to determine the ability of EC to characterize MTRs. In this work, we develop an algorithm to estimate the orientation distribution function of an MTR of interest using EC data. The method relies on an application of the central limit theorem, and the inverse problem is solved in using a likelihood-free technique. Numerical examples using simulated EC data are shown.

Keywords: microtexture region, eddy current, uncertainty quantification, likelihood free estimation

(Some figures may appear in colour only in the online journal)

## 1. Introduction

The performance of a metal is fundamentally linked to the characteristics of its microstructure. At this scale, the material is comprised of atoms arranged into regular crystalline structures known as grains. Individual grains are described by their size, shape, and orientation: collectively, these parameters give rise to macroscale material properties. Metals also display order

\* Author to whom any correspondence should be addressed.

beyond the scale of a grain. Many titanium alloys (e.g., Ti–6Al–4V, or Ti-64) exhibit spatial clustering of similarly oriented grains, forming what are known as microtextured regions (MTRs). Like grains, MTRs are described by their size, shape, and orientation and affect material performance as a function of their common spatial distribution as defined by a component orientation distribution function (cODF). Microtexture has profound implications for component fatigue life, driving early subsurface crack nucleation and accelerated crack growth ([12, 13, 18, 19]). Thus, a non-destructive method to detect and characterize MTRs is needed.

The device most commonly used for this task is a scanning electron microscope fitted with an electron backscatter diffraction (EBSD) detector, which is capable of measuring the orientation of surface grains (and their aggregation into MTR). However, EBSD has severe limitations for practical characterization of component-level microstructure; in particular, the sample needs to be flat with stringent (damage-free) surface preparation, and typically less than  $1'' \times 1''$  in area. In addition, the microscope itself is costly, and requires a highly-controlled testing environment. As such, an alternative, more practical technique is needed.

One potential method under investigation to solve this problem is eddy current (EC) testing, which is an electromagnetic technique that uses a primary magnetic field to generate a localized, secondary field within the inspected material. Local changes in conductivity that correlate to the local changes in grain orientation affect the impedance of the observed response. EC can reliably detect conductivity changes of 6% [4]. In addition, EC is a rapid and cost effective technique widely used for inspection of cracks in titanium components.

Using EC to characterize MTR comes with its own set of challenges. A single EC measurement can be thought of as an average of the electromagnetic fields within the test piece in the vicinity of the EC sensor. The smallest state-of-the-art EC sensors average over a region  $12\,000\times$  larger than individual grains. As a result, the EC data blurs the boundaries between neighboring regions. As such, the MTR characterization problem is split into two smaller problems. The first problem is to segment the underlying material into regions defined by different cODFs; then, given this segmentation, the second problem is to estimate each cODF. This paper will focus on the second problem. Thus, the question we seek to answer with this work is: given a segmentation of the material, what information about the underlying cODFs can be learned from EC impedance measurements of the material?

This paper is organized as follows: section 2 provides a detailed definition of the problem, section 3 details the methods, section 4 presents numerical results, and section 5 discusses conclusions and future work.

## 2. Definition of the problem

### 2.1. Microstructure of titanium

The majority of titanium alloys of interest to us consist primarily of grains with hexagonal close packed crystal structure, as seen in figure 1. The prism in figure 1 represents the unit cell of crystal orientation for grains that have hexagonal symmetry.

The crystallographic orientation is the set of rotations that describes the orientation of each grain with respect to the global frame of reference. Here it is defined in terms of three Euler angles  $(\psi_1, \theta, \psi_2)$ . Figure 1 provides an illustration. The first Euler angle,  $\psi_1$ , is a rotation about the original  $z$ -axis; this generates a new  $x$  and  $y$  axis. In the diagram, the new  $x$ -axis is labeled  $X'$ . The second Euler angle,  $\theta$ , is the subsequent rotation about the new  $x$ -axis,  $X'$ ; this generates a new  $z$ -axis, denoted  $Z'$  in the figure. The third Euler angle,  $\psi_2$ , is a rotation about the new  $z$ -axis. Note that  $\psi_1 \in [0, 2\pi]$ ,  $\theta \in [0, \pi]$ , and  $\psi_2 \in [0, 2\pi]$ . For more information on the microstructure of titanium, we refer to [4, 11].

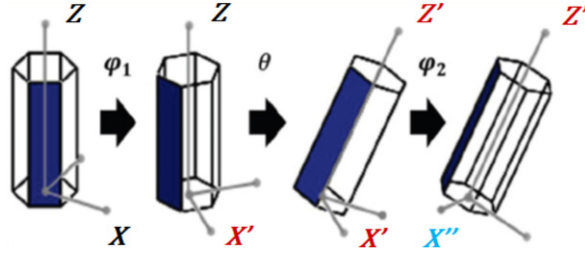


**Figure 1.** Rotations that correspond to the three Euler angles. The far left diagram shows the global frame of reference [5].

We can restrict the space of potential orientations using the symmetry of the hexagonal close packed crystal. In particular, for the hexagonal close packed crystal structure, the range of Euler angles needed to fully describe all potential crystallographic orientations is  $\psi_1 \in [0, 2\pi]$ ,  $\theta \in [0, \pi/2]$ , and  $\psi_2 \in [0, \pi/3]$  (see, for instance, [14]).

The sensitivity of the EC method also restricts how much information we can determine about the underlying crystallographic orientation of the material. The axis collinear with the Z-axis is referred to as the *c*-axis of the crystal; furthermore, the plane spanned by the *x* and *y* axes is referred to as the basal plane. In  $\alpha$ -titanium, conductivity is isotropic in the basal plane but differs along the *c*-axis. Since EC is sensitive to changes in conductivity, it is only sensitive to changes in crystallographic orientation that correspond to changes in the first and second Euler angle.

## 2.2. Definition of the ODF

For the purposes of this work, it will be assumed that the orientation of each grain is an independent realization of the random vector  $(\Psi_1, \Theta, \Psi_2)$ , whose joint probability distribution is given by the ODF. The ODF of the underlying material consists of several cODFs. Formally, if the underlying specimen  $V$  consists of  $p$  regions  $V_1, V_2, \dots, V_p$  such that

$$\bigcup_{h=1}^p V_h = V, \quad V_i \cap V_j = \emptyset, \quad i \neq j, \quad (1)$$

then the ODF can be written as

$$f(\psi_1, \theta, \psi_2 | x, y) = \begin{cases} f_1(\psi_1, \theta, \psi_2) & (x, y) \in V_1 \\ f_2(\psi_1, \theta, \psi_2) & (x, y) \in V_2 \\ \vdots & \\ f_p(\psi_1, \theta, \psi_2) & (x, y) \in V_p \end{cases}, \quad (2)$$

where  $f_h(\psi_1, \theta, \psi_2)$  is the cODF of the region  $V_h$ . It will be assumed in this work that each cODF is effectively a probability density function, implying that each cODF is strictly positive and integrates to one. Note that under this definition, estimating the ODF is equivalent to estimating each of the individual cODFs of each of the  $p$  regions in a fixed segmentation  $\{V_h\}_{h=1}^p$  of the underlying specimen. Due to the lack of sensitivity to the third Euler angle in the EC measurements, we are only able to estimate the marginal ODF of the first and second Euler

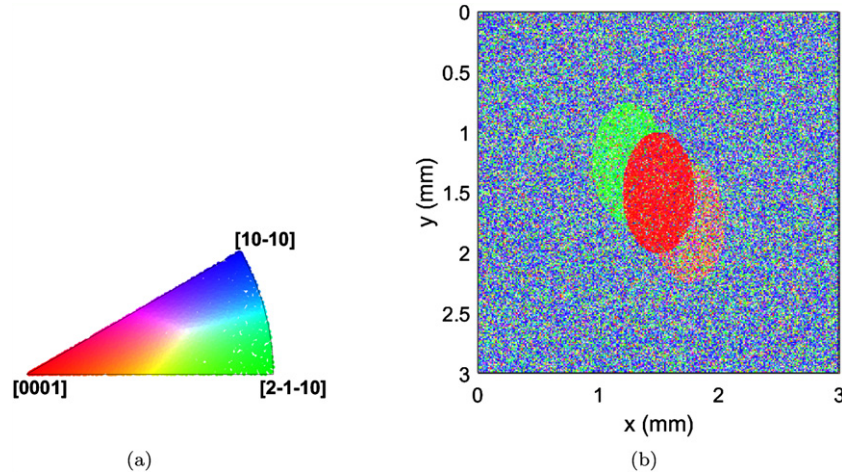


**Figure 2.** (a) Legend for the IPF map. (b) IPF map of a simulated specimen consisting of four cODFs; one cODF is contained in each of the three ellipses, and one is contained in the background region.

angles, which we will denote  $f(\psi_1, \theta|x, y)$ . The corresponding marginal cODFs are denoted  $f_h(\psi_1, \theta)$ .

### 2.3. IPF maps

The simulated specimens in this paper will be displayed using inverse pole figure (IPF) maps, which are a means of displaying the crystallographic orientation of each grain within a specimen using different colors. An example is shown in figure 2. Each pixel in the image corresponds to a different grain; the color of each pixel is representative of the crystallographic orientation of that grain, mapped into its equivalent symmetric orientation in the unit cell of the stereographic projection. The legend used for the IPF map is also shown in figure 2.

For the purpose of this work, the tilt of the  $c$ -axis of the hexagonal crystal (i.e. the second Euler angle,  $\theta$ ) has the most bearing on the EC signal. In these images,  $c$ -axis orientations that are close to vertical ( $\theta \approx 0$ ) are colored closer to red, and blue and green show orientations where the  $c$ -axis is lying in the plane of the specimen surface ( $\theta \approx \pi/2$ ). For further information on graphical representations of crystallographic orientation, we refer to [14].

The IPF map in figure 2 consists of four cODFs. The ellipse in the center of the specimen that contains primarily red pixels represents a basally-oriented MTR, where a majority of the crystallographic orientations have a second Euler angle close to zero. This is the type of MTR that we will be primarily concerned with in this work.

## 3. Methods

### 3.1. EC forward model

The forward model used to simulate data is the approximate impedance integral (AII) model [4], which makes use of the Born approximation and expresses the change in impedance as a volume integral. **The intent of the model is to predict the change of impedance of a coil due to the presence of crystallites in the sample whose conductivity varies randomly as a function of**

the orientation of the crystal. Starting with Maxwell's equations, Ampere's law and Faraday's law in differential form are given by

$$\begin{aligned}\nabla \times \mathbf{H} &= j\omega\varepsilon\mathbf{E} + \bar{\sigma} \cdot \mathbf{E} \\ \nabla \times \mathbf{E} &= -j\omega\mu\mathbf{H}.\end{aligned}\quad (3)$$

In these equations,  $\omega$  is the angular frequency,  $\mu$  is the permeability,  $\varepsilon$  is the scalar permittivity, and  $\bar{\sigma}$  is the anisotropic conductivity tensor. It is assumed that there are no external fields and that the only source of currents is the induced current density in the conductive media and displacement currents. These equations can be combined [2] by taking the dot product of the first equation with  $\mathbf{E}$  and the second equation with  $\mathbf{H}$  to give

$$\oint_S (\mathbf{E} \times \mathbf{H}) \cdot \mathbf{n} dS = \int_V [j\omega\mu\mathbf{H} \cdot \mathbf{H} + j\omega\varepsilon\mathbf{E} \cdot \mathbf{E} + \mathbf{E} \cdot (\bar{\sigma} \cdot \mathbf{E})] dV \quad (4)$$

where  $S$  is the surface enclosing a flaw in the conductive media and  $V$  is the volume of that flaw. In the case of an anisotropic microstructure,  $S$  is the surface around the entire sample itself.

An important review article [1] describes a process for deriving the impedance of a coil in the presence of a conductive sample with a defect. If we denote the fields resulting from exciting a coil in the presence of an isotropic half-space with conductivity  $\sigma_a$  with an  $a$  subscript, and the fields resulting from exciting the coil above an anisotropic, polycrystalline sample with a  $b$  subscript, the impedance of the coil can be expressed as

$$\begin{aligned}\Delta Z &= \frac{1}{I^2} \int_V [j\omega\mu(\mathbf{H}_a \cdot \mathbf{H}_a - \mathbf{H}_b \cdot \mathbf{H}_b) + j\omega\varepsilon(\mathbf{E}_a \cdot \mathbf{E}_a - \mathbf{E}_b \cdot \mathbf{E}_b) \\ &\quad + \mathbf{E}_a \cdot (\sigma_a \mathbf{I}_{3 \times 3} \cdot \mathbf{E}_a) - \mathbf{E}_b \cdot (\bar{\sigma}_b \cdot \mathbf{E}_b)] dV.\end{aligned}\quad (5)$$

In this equation,  $I$  is the current applied to the coil and  $\mathbf{I}_{3 \times 3}$  is the  $3 \times 3$  identity matrix.

If we assume that the change in conductivity from the anisotropic polycrystalline sample to the reference state is small, the Born approximation can be applied to (5). The Born approximation essentially assumes that the fields inside the scatterer (or crystallites, in this case), is equal to the field in the reference isotropic state. In other words, the field values with  $a$  subscripts are equal to the field values with  $b$  subscripts in the scatterer regions. This allows us to finally write the model as

$$\Delta Z(\psi_1, \theta) = \frac{1}{I^2} \int_V \mathbf{E}_a^T (\sigma_a \mathbf{I}_{3 \times 3} - \bar{\sigma}_b(\psi_1, \theta)) \mathbf{E}_a dV, \quad (6)$$

where  $\bar{\sigma}_b$  is the rotated conductivity tensor, and  $\psi_1$  and  $\theta$  are the first and second Euler angles, respectively. The rotated conductivity tensor  $\bar{\sigma}_b$  is a function of the local crystallographic orientation and is given by

$$\bar{\sigma}_b = \begin{bmatrix} \sigma_{11} & \sigma_{12} & \sigma_{13} \\ \sigma_{12} & \sigma_{22} & \sigma_{23} \\ \sigma_{13} & \sigma_{23} & \sigma_{33} \end{bmatrix}, \quad (7)$$

where

$$\begin{aligned}\sigma_{11} &= \sigma_{xx} + (\sigma_{zz} - \sigma_{xx})s_1^2s_2^2 & \sigma_{12} &= s_1c_1s_2^2(\sigma_{xx} - \sigma_{zz})/2 \\ \sigma_{13} &= -s_1c_2s_2(\sigma_{xx} - \sigma_{zz}) & \sigma_{22} &= \sigma_{xx} + (\sigma_{zz} - \sigma_{xx})s_2^2 + (\sigma_{xx} - \sigma_{zz})s_1^2s_2^2 \\ \sigma_{23} &= c_1c_2s_2(\sigma_{xx} - \sigma_{zz}) & \sigma_{33} &= \sigma_{zz} + (\sigma_{xx} - \sigma_{zz})s_2^2\end{aligned}$$

and  $c_i$  and  $s_i$  are the sine and cosine of the  $i$ th Euler angle, respectively. For further details on this model, we refer to [4]. Within this work, these expressions will be treated as functions. For instance, we let

$$\sigma_{11}(\psi_1, \theta) = \sigma_{xx} + (\sigma_{zz} - \sigma_{xx}) \sin^2(\psi_1) \sin^2(\theta).$$

### 3.2. Likelihood free inference

One of the major challenges of the ODF estimation problem is the lack of an available forward model that takes as input the underlying cODFs and produces as output a set of EC data. That is, even if we knew the exact cODFs of the material, we could not recreate the measured EC data. As such, we cannot construct a likelihood function, and are unable to use traditional Bayesian estimation for this problem. Thus, we need a different approach.

To solve the ODF estimation problem, we instead turn to likelihood free estimation (see, for instance, [9, 16]). Recall that in traditional Bayesian estimation, the solution to the inverse problem is given by the posterior distribution of the unknown given the measured data, that is,

$$\pi_{\text{post}}(\xi|z) \propto \pi(z|\xi)\pi_{\text{prior}}(\xi), \quad (8)$$

where  $\xi$  is the unknown of interest,  $z$  is the measured data,  $\pi(z|\xi)$  is the likelihood distribution of the data given a fixed value of the unknown and  $\pi_{\text{prior}}(\xi)$  is the prior distribution of the unknown. The likelihood distribution accounts for any deviation between the forward model and the measured data, while the prior distribution incorporates any information we have about the unknown before taking into account the data.

With likelihood free inference, the usual posterior distribution is augmented using an auxiliary parameter  $\rho$ , that is,

$$\pi_{\text{LF}}(\xi, \rho|z) \propto \pi(z|\xi, \rho)\pi(\rho|\xi)\pi(\xi), \quad (9)$$

where  $\rho$  is a simulated dataset drawn from  $\pi(\rho|\xi)$ . The function  $\pi(z|\xi, \rho)$  is a weighting function which attains high values when  $\rho$  is close to  $z$ . As mentioned in [16], this weighting function can take on a number of different forms.

As noted in [16], the weighting function  $\pi(z|\xi, \rho)$  is meant to compare the simulated dataset  $\rho$  to the measured dataset  $z$ . This can be achieved by either comparing the two datasets directly, or by comparing a set of summary statistics from each of the datasets. For the ODF estimation problem, we make use of summary statistics.

The distribution  $\pi(\rho|\xi)$  is a means of generating simulated datasets (or pseudo-observations, see [6])  $\rho$  for a fixed value of the unknown. An example of how this distribution is chosen is shown on a toy example in [6]. For our application, we do not generate any pseudo-observations, as the summary statistics needed for the inversion can be computed directly from a set of candidate cODFs. As such, this distribution does not factor into our inversion.

In order to sample from the augmented posterior, we use a variant of the Metropolis–Hastings algorithm. The likelihood free Metropolis–Hastings algorithm is quite similar to the traditional algorithm, with the exception that the likelihood function is replaced by the weighting function in the probability for accepting a proposed move. We refer to [9, 16] for further details.

In addition to sampling from the augmented posterior, we will also look at single point estimates of the ODF. In particular, we will consider the maximum *a posteriori* (MAP) estimate, which in the likelihood free context is given by

$$(\xi, \rho)_{\text{MAP}} = \arg \max \pi_{\text{LF}}(\xi, \rho|z),$$



that is, the value of the unknown that maximizes the augmented posterior.

### 3.3. Application of likelihood-free estimation to ODF estimation

We begin formulating summary statistics for use in the likelihood free method by observing that the EC responses due to a known ODF follow a normal distribution. The orientations of the grains located beneath the EC coil are independent realizations of the random vector  $(\Psi_1, \Theta, \Psi_2|x, y)$ , which obeys the distribution given by the cODF of the region where  $(x, y)$  is located. The local conductivity is a random variable, as it is a function of the local crystallographic orientation. The EC response due to each region is loosely an average of the local conductivity values within that region, implying that it is an average of independent, identically distributed random variables, in which case the central limit theorem applies. More specifically, both the real and imaginary EC responses due to a known ODF follow a normal distribution; thus, we will model the noiseless real and imaginary EC responses as realizations of two normal random variables.

**3.3.1. Data model.** Let  $\tilde{z} \in \mathbb{C}^m$  denote a vector of noiseless EC measurements. Note that since  $\tilde{z}$  is complex, we will express it as

$$\tilde{z} = \tilde{z}_{\text{re}} + j\tilde{z}_{\text{im}}, \quad (10)$$

where  $\tilde{z}_{\text{re}} \in \mathbb{R}^m$  and  $\tilde{z}_{\text{im}} \in \mathbb{R}^m$  denote the real and imaginary parts of  $\tilde{z}$ , respectively. Applying the central limit theorem, we model  $\tilde{z}_{\text{re}}$  and  $\tilde{z}_{\text{im}}$  as realizations of two normally distributed random variables  $Z_{\text{re}}$  and  $Z_{\text{im}}$ ,

$$Z_{\text{re}} \sim N(\mu_{\text{re}}, \tilde{\Gamma}_{\text{re}}), \quad Z_{\text{im}} \sim N(\mu_{\text{im}}, \tilde{\Gamma}_{\text{im}}), \quad (11)$$

where, for instance,  $\mu_{\text{re}} \in \mathbb{R}^m$  and  $\tilde{\Gamma}_{\text{re}} \in \mathbb{R}^{m \times m}$  are the mean and covariance matrix of the real EC response due to a fixed ODF  $f(\psi_1, \theta|x, y)$ , that is

$$\begin{aligned} \mu_{\text{re}} &= \mathbb{E} [Z_{\text{re}}|f(\psi_1, \theta|x, y)], \quad \tilde{\Gamma}_{\text{re}} = \mathbb{E} [(Z_{\text{re}} - \mu_{\text{re}})(Z_{\text{re}} - \mu_{\text{re}})^T \\ &\quad \times |f(\psi_1, \theta|x, y)]. \end{aligned} \quad (12)$$

The terms  $\mu_{\text{im}} \in \mathbb{R}^m$  and  $\tilde{\Gamma}_{\text{im}} \in \mathbb{R}^{m \times m}$  are defined similarly. A discussion of how  $\mu_{\text{re}}$ ,  $\mu_{\text{im}}$ , and  $\tilde{\Gamma}_{\text{re}}$ ,  $\tilde{\Gamma}_{\text{im}}$  are computed for a fixed ODF is provided later in this section.

Now, let  $z \in \mathbb{C}^m$  denote a vector of EC measurements, with measurement noise. The complete model for the real portion of  $z$  is then

$$z_{\text{re}} = \mu_{\text{re}} + \omega_{\text{re}} + \epsilon_{\text{re}}, \quad \omega_{\text{re}} \sim N(0, \tilde{\Gamma}_{\text{re}}), \quad \epsilon_{\text{re}} \sim N(0, \delta_{\text{re}}^2 \mathbf{I}), \quad (13)$$

where the term  $\epsilon_{\text{re}} \in \mathbb{R}^m$  represents iid measurement noise on the real portion of the measurements. Similarly, for  $z_{\text{im}}$ , we may write

$$z_{\text{im}} = \mu_{\text{im}} + \omega_{\text{im}} + \epsilon_{\text{im}}, \quad \omega_{\text{im}} \sim N(0, \tilde{\Gamma}_{\text{im}}), \quad \epsilon_{\text{im}} \sim N(0, \delta_{\text{im}}^2 \mathbf{I}), \quad (14)$$

**3.3.2. Computation of necessary quantities.** The quantities  $\mu_{\text{re}}$ ,  $\mu_{\text{im}}$ , and  $\tilde{\Gamma}_{\text{re}}$ ,  $\tilde{\Gamma}_{\text{im}}$  can be computed for a fixed ODF and segmentation of the specimen  $\{V_h\}_{h=1}^p$  using the AII model. First, let  $\tilde{z}_\ell$  denote the noiseless EC measurement at measurement location  $(x_\ell, y_\ell)$ . Using the AII model, we have that



$$\begin{aligned}\tilde{z}_\ell &= \frac{1}{I^2} \int_V (\mathbf{E}_a^\ell)^T (\sigma_a \mathbf{I}_{3 \times 3} - \bar{\sigma}_b(\psi_1, \theta)) \mathbf{E}_a^\ell dV \\ &= \frac{1}{I^2} \sum_{h=1}^p \int_{V_h} (\mathbf{E}_a^\ell)^T (\sigma_a \mathbf{I}_{3 \times 3} - \bar{\sigma}_b(\psi_1, \theta)) \mathbf{E}_a^\ell dV,\end{aligned}$$

where  $\mathbf{E}_a^\ell$  is the incident electric field when the EC coil is centered at  $(x_\ell, y_\ell)$ . Let

$$\mu_\ell = \frac{1}{I^2} \sum_{h=1}^p \int_{V_h} (\mathbf{E}_a^\ell)^T (\sigma_a \mathbf{I}_{3 \times 3} - \mathbb{E}_{f_h} [\bar{\sigma}_b(\psi_1, \theta)]) \mathbf{E}_a^\ell dV,$$

where  $\mathbb{E}_{f_h} [\bar{\sigma}_b(\psi_1, \theta)]$  is the calculated by taking the expectation of each term in  $\bar{\sigma}_b(\psi_1, \theta)$  with respect to  $f_h$ . Then the  $\ell$ th entries of  $\boldsymbol{\mu}_{\text{re}}$  and  $\boldsymbol{\mu}_{\text{im}}$  are given by the real and imaginary portions of  $\mu_\ell$ , respectively. Similarly, let

$$\gamma_\ell^2 = \sum_{h=1}^p \int_{\mathbb{R}^2} \left( \int_{V_h} (\mathbf{E}_a^\ell)^T (\sigma_a \mathbf{I}_{3 \times 3} - \bar{\sigma}_b(\psi_1, \theta)) \mathbf{E}_a^\ell dV \right)^2 f_h(\psi_1, \theta) d\theta d\psi_1 - \mu_\ell^{(h)^2}, \quad (15)$$

where

$$\mu_\ell^{(h)} = \int_{V_h} (\mathbf{E}_a^\ell)^T (\sigma_a \mathbf{I}_{3 \times 3} - \mathbb{E}_{f_h} [\bar{\sigma}_b(\psi_1, \theta)]) \mathbf{E}_a^\ell dV. \quad (16)$$

The  $\ell$ th diagonal entries of  $\tilde{\Gamma}_{\text{re}}$  and  $\tilde{\Gamma}_{\text{im}}$  are given by the real and imaginary portions of  $\gamma_\ell^2$ , respectively. The off-diagonal entries of  $\tilde{\Gamma}_{\text{re}}$  and  $\tilde{\Gamma}_{\text{im}}$  are computed similarly. In particular, let

$$\begin{aligned}\gamma_{\ell k} &= \sum_{h=1}^p \int_{\mathbb{R}^2} \left( \int_{V_h} g(\mathbf{E}_a^\ell, \bar{\sigma}_b) dV \int_{V_h} g(\mathbf{E}_a^k, \bar{\sigma}_b) dV \right) \\ &\quad \times f_h(\psi_1, \theta) d\theta d\psi_1 - \mu_\ell^{(h)} \mu_k^{(h)}\end{aligned} \quad (17)$$

where

$$g(\mathbf{E}_a^\ell, \bar{\sigma}_b) = (\mathbf{E}_a^\ell)^T (\sigma_a \mathbf{I}_{3 \times 3} - \bar{\sigma}_b(\psi_1, \theta)) \mathbf{E}_a^\ell. \quad (18)$$

Then the  $(\ell, k)$  and  $(k, \ell)$  entries of  $\tilde{\Gamma}_{\text{re}}$  and  $\tilde{\Gamma}_{\text{im}}$  are given by the real and imaginary portions, respectively, of  $\gamma_{\ell k}$ .

The last quantity that will be required for the inversion is the covariance matrix between the real and imaginary portions of the signal, which we will denote  $\hat{\Gamma} \in \mathbb{R}^{m \times m}$ . The entries of  $\hat{\Gamma}$  are given by

$$\begin{aligned}\hat{\gamma}_{\ell k} &= \sum_{h=1}^p \int_{\mathbb{R}^2} \left( \int_{V_h} \text{Re}(g(\mathbf{E}_a^\ell, \bar{\sigma}_b)) dV \int_{V_h} \text{Im}(g(\mathbf{E}_a^k, \bar{\sigma}_b)) dV \right) \\ &\quad \times f_h(\psi_1, \theta) d\theta d\psi_1 - \text{Re}(\mu_\ell^{(h)}) \text{Im}(\mu_k^{(h)}),\end{aligned} \quad (19)$$

where  $\text{Re}(\cdot)$  and  $\text{Im}(\cdot)$ , respectively, denote the real and imaginary portions of a given quantity. Note that unlike  $\Gamma_{\text{re}}$  and  $\Gamma_{\text{im}}$ ,  $\hat{\Gamma}$  is not symmetric. Each of the terms  $\mu_\ell$ ,  $\gamma_\ell^2$ ,  $\gamma_{\ell k}$ , and  $\hat{\gamma}_{\ell k}$  is computed numerically.

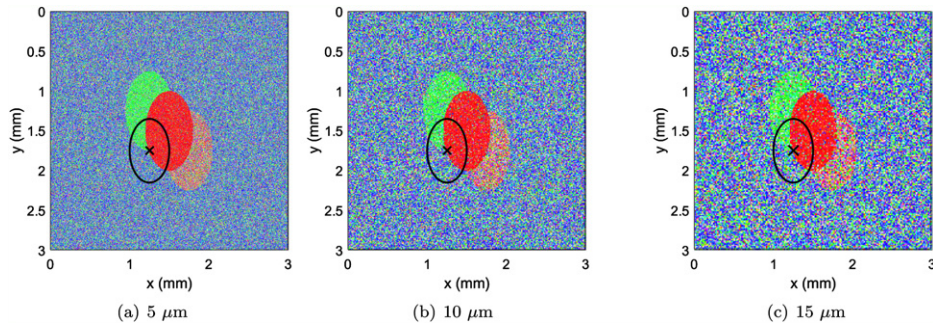


**Figure 3.** IPF maps of simulated specimens with grain sizes of (a) 5  $\mu\text{m}$ , (b) 10  $\mu\text{m}$  and (c) 15  $\mu\text{m}$ . The cODFs for each region are the same in each specimen. The black ‘x’ indicates the location of the EC coil to generate the results in figure 4.

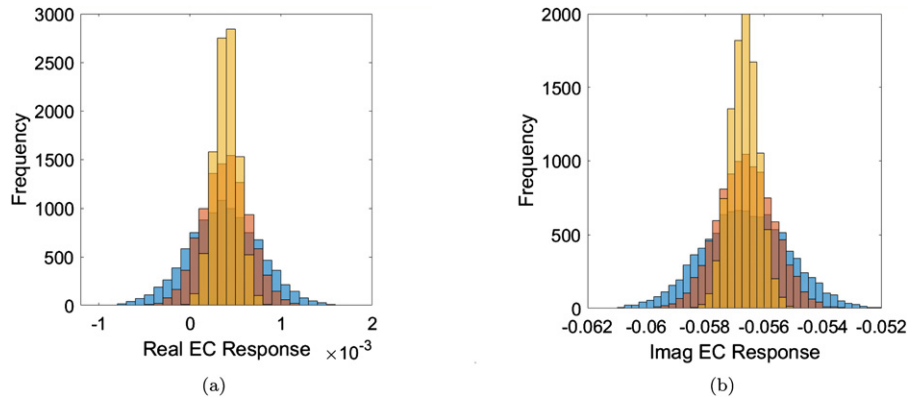


**Figure 4.** Computed distributions of EC responses for the same ODF assuming three different grain sizes. The blue histogram is for the 15  $\mu\text{m}$  grain size, red is 10  $\mu\text{m}$ , and yellow is 5  $\mu\text{m}$ . Shown are (a) the real EC response, (b) the imaginary response.

**3.3.3. Relation to grain size.** It should be noted that the variance and covariance of the EC responses due to a given ODF are dependent on the assumed grain size. Here, grain size refers to the edge size of a square pixel defined by a single orientation.

Figure 3 shows three specimens with the same four regions and cODFs, but with different grain sizes. Note that all grains within a single simulated specimen are the same size. The grain orientations within each specimen were re-sampled from their respective cODFs, and an EC measurement was simulated with the coil centered at the black ‘x’ shown in figure 3. This process was repeated 10 000 times. The resulting histograms of the real and imaginary EC responses are shown in figure 4. **Note that while the mean of each distribution remains the same, the standard deviation of the responses decreases along with the grain size.**

**This result is not surprising if we consider the central limit theorem. Recall that the central limit theorem tells us that the average of a random sample of size  $n$  from a distribution with mean  $\mu$  and variance  $\sigma^2$  follows a normal distribution with mean  $\mu$  and variance  $\sigma^2/n$ . That is, the variance of normal distribution decreases as the sample size  $n$  increases. From the EC perspective, as the grain size decreases, the number of grains beneath the EC coil increases, and**

thus the number of grains that the coil averages over increases. This results in lower variability in the EC measurement as the grain size decreases.

In this work, the assumed grain size corresponds to the spatial discretization size used in the numerical integration to compute the expressions in (15), (17) and (19); as such, the computed values of these quantities are dependent on the assumed grain size. In particular, let  $\gamma_\ell^2(f(\psi_1, \theta), g)$  denote (15) computed for the ODF  $f(\psi_1, \theta)$  with grain size  $g$ . Then, using the central limit theorem, it can be shown that

$$\gamma_\ell^2(f(\psi_1, \theta), g/s) = \frac{\gamma_\ell^2(f(\psi_1, \theta), g)}{s^2}, \quad (20)$$

where  $s$  is any positive real number. This relationship also holds for (17) and (19).

The parameter  $s$  must be set in the inversion algorithm; it represents the ratio between the grain size used for computing (15), (17) and (19) and the true grain size. Because in our simulations the true grain size is known (and constant),  $s$  is fixed. However, when dealing with realistic specimens, the grain size will not be known. In that case,  $s$  will become an unknown to be estimated in the inverse problem. Methods to estimate  $s$  when the grain size is unknown will be a topic of future research.

**3.3.4. Summary statistics for EC data.** Having established the statistical characteristics of the data, we can now formulate the summary statistics for the likelihood-free technique. In the remaining calculations, we denote

$$\Gamma_{\text{re}} = \tilde{\Gamma}_{\text{re}} + \delta_{\text{re}}^2 \mathbf{I}, \quad \Gamma_{\text{im}} = \tilde{\Gamma}_{\text{im}} + \delta_{\text{im}}^2 \mathbf{I}. \quad (21)$$

In addition, let

$$\zeta = \begin{bmatrix} z_{\text{re}} \\ z_{\text{im}} \end{bmatrix}, \quad b = \begin{bmatrix} \mu_{\text{re}} \\ \mu_{\text{im}} \end{bmatrix}, \quad \Lambda = \begin{bmatrix} \Gamma_{\text{re}} & \hat{\Gamma} \\ \hat{\Gamma}^T & \Gamma_{\text{im}} \end{bmatrix}.$$

For  $\mu_{\text{re}}$ ,  $\mu_{\text{im}}$ ,  $\Gamma_{\text{re}}$ ,  $\Gamma_{\text{im}}$ , and  $\hat{\Gamma}$  computed using the set of cODFs that generated  $z$ , we have

$$\zeta \sim N(b, \Lambda).$$

Furthermore, observe that for the Cholesky factor  $R$  of  $\Lambda$ ,

$$w = R^{-T}(\zeta - b) \sim N(0, \mathbf{I}),$$

and it is known that for a standard normal random vector  $w \in \mathbb{R}^{2m}$ ,

$$\mathbb{E}[\|w\|] \approx \sqrt{2m}.$$

This is the basis for our first summary statistic. In particular, for a candidate ODF  $\hat{f}(\psi_1, \theta)$ , we calculate

$$w_{\hat{f}} = R_{\hat{f}}^{-T}(\zeta - b_{\hat{f}}), \quad \Lambda_{\hat{f}} = R_{\hat{f}}^T R_{\hat{f}},$$

where  $b_{\hat{f}}$  and  $\Lambda_{\hat{f}}$  are the mean and covariance matrix, respectively, of the EC responses computed using  $\hat{f}$ . For a choice of  $\hat{f}$  that is close to the true ODF of the material, the norm of  $w_{\hat{f}}$  will be approximately  $\sqrt{2m}$ . This will be formalized in the weighting function for the problem, described in the next section.

Moreover, due to the central limit theorem, the mean of the components of a standard normal random vector  $w \in \mathbb{R}^{2m}$  follows a normal distribution,

$$\bar{w} \sim N\left(0, \frac{1}{2m}\right), \quad (22)$$

where  $\bar{w}$  denotes the mean of the components of  $w$ . Thus, for a candidate ODF  $\hat{f}$ , the second summary statistic is the mean of  $w_{\hat{f}}$ . If  $\hat{f}$  is similar to the true ODF of the material, then the mean of  $w_{\hat{f}}$  should be approximately equal to 0.

Thus, the two summary statistics that we will use in the ODF inversion are  $\|w_{\hat{f}}\|$  and  $\bar{w}_{\hat{f}}$ .

**3.3.5. Weighting function.** Having established the summary statistics for the inversion, we now formulate the weighting function. As mentioned in [16], while the weighting functions can take on several different forms, it is important to account for the known distribution of any of the summary statistics. For our application, the mean of a standard normal random vector follows a normal distribution (per the central limit theorem). It can also be shown empirically that the norm of a standard normal random vector follows a normal distribution. **Thus, we use a Gaussian weighting function for the inversion, that is**

$$\pi(z|f, \|w_f\|, \bar{w}_f) = \exp\left(-2m(\bar{w}_f^2) - \frac{(\|w_f\| - \sqrt{2m})^2}{\sigma_{\text{norm}}^2}\right), \quad (23)$$

where  $\sigma_{\text{norm}}$  is the standard deviation of the norm of a standard normal random vector of length  $2m$ .

**3.3.6. Prior distribution.** It is assumed that the unknown cODFs are independent, so that their joint prior distribution can be expressed as

$$\pi_{\text{prior}}(f) = \pi_{\text{prior}}(f_1, \dots, f_p) = \prod_{h=1}^p \pi_{\text{prior}}(f_h). \quad (24)$$

The prior distribution  $\pi_{\text{prior}}(f_h)$  restricts the choices of  $f_h$  to functions that are strictly greater than or equal to zero, and integrate to one. However, the prior is otherwise non-informative in order to prevent bias in the MAP estimates. Further details about the prior distribution for specific parametric forms of the cODFs will be given in the numerical results section.

## 4. Numerical examples

### 4.1. Simulated data

We demonstrate the ODF estimation algorithm on two simulated datasets. The first dataset, shown in figure 5, was meant to emulate data from an MTR. Specifically, we simulated a specimen containing an elliptical MTR with a predominantly basal orientation embedded within another region that is non-basal; the IPF map of this simulated specimen is also shown in figure 5. This dataset is comprised of two cODFs; note that both cODFs were simulated using the model in [17]. The second dataset, shown in figure 6, consists of four cODFs, and includes an MTR that is roughly one quarter of the size of the elliptical MTR in figure 5. As with the first dataset, each of the cODFs was simulated using the model in [17].

In both cases, the data was simulated using the AII model with a simulated elliptical EC coil, with semi-axes  $250 \mu\text{m}$  and  $750 \mu\text{m}$ . The liftoff of the coil was  $100 \mu\text{m}$ . The incident

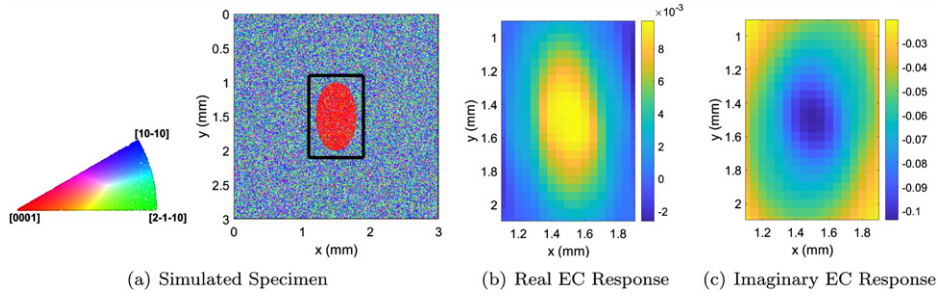


**Figure 5.** Simulated EC data for demonstration of ODF estimation. (a) IPF map of the simulated specimen. The black outline indicates the measurement region. (b)–(c) The real and imaginary portions of the simulated data.

electric field due to this coil was simulated using COMSOL. To each dataset, we added white Gaussian noise with standard deviation equal to 1% of the maximum of the absolute value of the noiseless scan. Note that noise was added separately to the real and imaginary portions of the data. For instance, the standard deviation of the noise added to the real portion is equal to 1% of the maximum of absolute value of the real portion of the data.

In both cases, the data was generated using a spatial discretization of 12  $\mu\text{m}$  in both the  $x$  and  $y$  directions; that is, the true grain size is 12  $\mu\text{m}$ . To avoid an inverse crime, the inverse problem is solved using a spatial discretization of 24  $\mu\text{m}$ . Note that when solving the inverse problem, it is assumed that the boundaries of each region defined by a different cODF were known and fixed.

#### 4.2. Parametric distribution

In the inverse problem, it is assumed that each of the cODFs can be represented using the Bingham distribution. The Bingham distribution is expressed in terms of quaternions; the quaternion vector, in terms of Euler angles, is defined as

$$q = \left[ \cos\left(\frac{\theta}{2}\right) \cos(\alpha), -\sin\left(\frac{\theta}{2}\right) \cos(\beta), -\sin\left(\frac{\theta}{2}\right) \sin(\beta), -\cos\left(\frac{\theta}{2}\right) \sin(\alpha) \right], \quad (25)$$

where  $\alpha = \frac{1}{2}(\psi_1 + \psi_2)$  and  $\beta = \frac{1}{2}(\psi_1 - \psi_2)$ . For more information on quaternions and other alternate representations of crystallographic orientation, we refer to [15]. The pdf for the Bingham distribution is given by

$$\pi(x) \propto \exp\left(\sum_{i=1}^4 \lambda_i (v_i^T x)^2\right), \quad (26)$$

where  $x$  is a unit quaternion,  $v_i \in \mathbb{R}^4$ ,  $1 \leq i \leq 4$  are four orthonormal directions, and  $\lambda_i \leq 0$ ,  $1 \leq i \leq 4$ . As noted in [10], this definition is ambiguous; as such, we use the following conventions. In this work, we will let  $v_1 = q$ , where  $q$  is as defined in (25). **Due to the lack of EC sensitivity to the third Euler angle  $\psi_2$ , we set  $\psi_2 = 0$  in all of our calculations.** The vectors  $v_2$  and  $v_3$  are the partial derivatives with respect to  $\psi_1$  and  $\theta$ , respectively. We assume that  $\lambda_1 \geq \lambda_2 \geq \lambda_3$  and  $\lambda_4 = 0$ .

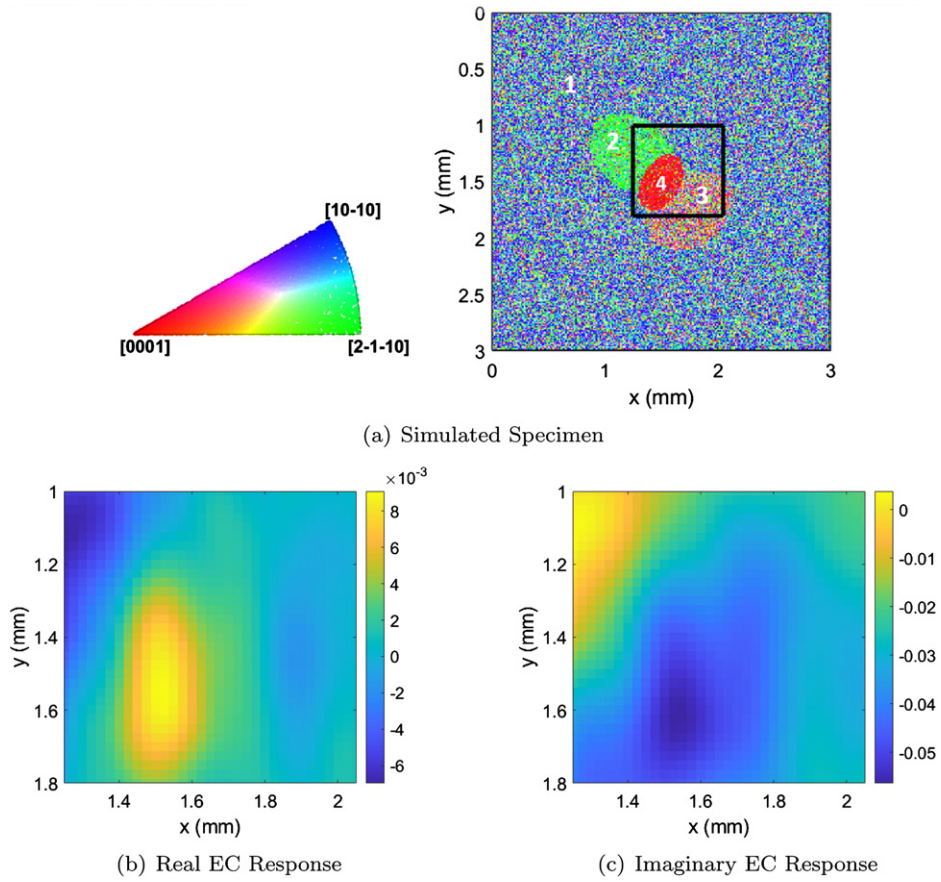


**Figure 6.** Simulated EC data for demonstration of ODF estimation. (a) IPF map of the simulated specimen. The black outline indicates the measurement region. (b)–(c) The real and imaginary portions of the simulated data.

Here we will only use a single Bingham distribution to represent each cODF; as noted in [10], if a cODF is too complex to be described by a single Bingham distribution, a finite mixture of Bingham distributions may be used instead.

#### 4.3. Prior distribution

Each Bingham distribution used to describe a cODF is described by five parameters:  $\mu_\psi$ ,  $\mu_\theta$ , and  $\lambda_1$ ,  $\lambda_2$ , and  $\lambda_3$ . Then

$$v_1 = \left[ \cos\left(\frac{\mu_\theta}{2}\right) \cos\left(\frac{\mu_\psi}{2}\right), -\sin\left(\frac{\mu_\theta}{2}\right) \cos\left(\frac{\mu_\psi}{2}\right), -\sin\left(\frac{\mu_\theta}{2}\right) \sin\left(\frac{\mu_\psi}{2}\right), -\cos\left(\frac{\mu_\theta}{2}\right) \sin\left(\frac{\mu_\psi}{2}\right) \right], \quad (27)$$

and

$$v_2 = \frac{\partial v_1}{\partial \mu_\psi}, \quad v_3 = \frac{\partial v_1}{\partial \mu_\theta}, \quad (28)$$



and the pdf of the distribution is given in (26).

As noted in [10], the parameters  $\lambda_1, \lambda_2, \lambda_3$  are only unique up to an additive constant. That is, the parameters  $\lambda_1, \lambda_2, \lambda_3$  will produce the same distribution as  $\lambda_1 + c, \lambda_2 + c, \lambda_3 + c$  for any  $c \in \mathbb{R}$  and  $\lambda_1, \lambda_2, \lambda_3 \neq 0$ . As such, we will assume that one of these parameters is fixed in inverse problem; specifically, we fix  $\lambda_1 = -0.5$ . The reason behind this choice is so that the values of  $\mu_\psi$  and  $\mu_\theta$  will have the most weight in the distribution. Note that by fixing  $\lambda_1 = -0.5$ , we are eliminating the possibility that  $\lambda_1 = \lambda_2 = \lambda_3 = 0$ , which corresponds to the uniformly distributed orientations. However, we have found that the distribution defined by  $\lambda_1 = \lambda_2 = \lambda_3 = -0.5$  is sufficiently close to uniform for our purposes.

Rather than estimate  $\lambda_2$  and  $\lambda_3$  directly, we introduce the auxiliary parameters

$$\eta = \frac{\lambda_1}{\lambda_2}, \quad \kappa = \frac{\lambda_2}{\lambda_3}.$$

These are the parameters that will be estimated in the inverse problem. This choice allows us to naturally accommodate the requirement that  $\lambda_1 \geq \lambda_2 \geq \lambda_3$  in the inverse problem.

The parameters for any of the  $p$  cODFs are assumed independent of the all other cODFs; furthermore, each of the four parameters describing a single cODF are assumed independent. Let

$$\nu_h = [\mu_\psi^h, \mu_\theta^h, \eta^h, \kappa^h] \quad (29)$$

denote the set of the parameters for the  $h$ th cODF. Then the prior distribution for the unknowns is given by

$$\pi_{\text{prior}}(\nu_1, \nu_2, \dots, \nu_p) = \prod_{h=1}^p \pi_{\text{prior}}(\nu_h), \quad (30)$$

and

$$\pi_{\text{prior}}(\nu_h) = \pi(\mu_\psi^h) \pi(\mu_\theta^h) \pi(\eta^h, \kappa^h). \quad (31)$$

Several combinations of  $(\eta, \kappa)$  produce Bingham distributions which appear mostly uniform and thus qualitatively similar, especially in the marginal distribution of the second Euler angle. In addition, some combinations of  $(\eta, \kappa)$  result in a Bingham distributions that essentially devolve to one point. Hence, the joint prior for  $(\eta, \kappa)$  is constructed to avoid combinations of  $(\eta, \kappa)$  that fall into either of these categories. Figure 7 shows the maximum value of the marginal distribution of the second Euler angle plotted for different combinations of  $\eta$  and  $\kappa$ . The region between the two black curves corresponds to the desirable combinations of  $\eta$  and  $\kappa$ .

The prior for  $(\eta, \kappa)$  is thus given by

$$\pi(\eta, \kappa) = \begin{cases} \exp(-(\kappa - u_1(\eta))^2) & \kappa > u_1(\eta) \\ 1 & \kappa \leq u_1(\eta), \kappa \geq u_2(\eta) \\ \exp(-(\kappa - u_2(\eta))^2) & \kappa < u_2(\eta) \end{cases} \quad (32)$$

Note that restricting the choices of  $\eta$  and  $\kappa$  to this area does not eliminate the possibility that the distribution could be nearly uniform, it simply eliminates redundant combinations of  $\eta$  and  $\kappa$ .



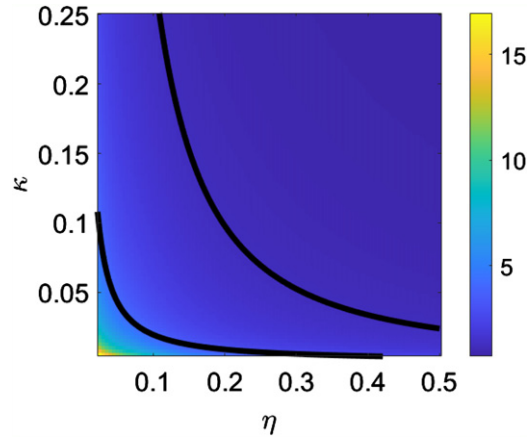


**Figure 7.** Image showing the maximum value of the marginal distribution of the second Euler angle using a Bingham distribution for varying values of  $\eta$  and  $\kappa$ . The region between the two black curves represents the desirable combinations of  $\eta$  and  $\kappa$ . The top curve is  $u_1$  in (32); the bottom curve is  $u_2$ .

We use a similar approach for the prior of  $\mu_\theta$ . Although  $\mu_\theta \in [0, \pi/2]$ , we found that for values of  $\mu_\theta$  close to 0, the resulting Bingham distributions are qualitatively similar. This pattern is also true as  $\mu_\theta$  approaches  $\pi/2$ . As a result, we use a prior for  $\mu_\theta$  that discourages values close to 0 and  $\pi/2$ . Specifically, the prior for  $\mu_\theta$  is

$$\pi(\mu_\theta) = \begin{cases} \exp\left(-\left(\frac{\mu_\theta - \pi/4}{1.05}\right)^{20}\right) & 0 \leq \mu_\theta \leq 0.1 \\ 1 & 0.1 < \mu_\theta < \pi/2 - 0.1 \\ \exp\left(-\left(\frac{\mu_\theta - \pi/4}{1.05}\right)^{20}\right) & \pi/2 - 0.1 \leq \mu_\theta \leq \pi/2 \end{cases} \quad (33)$$

Lastly, the prior for  $\mu_\psi$  is uniform on the interval  $[0, \pi]$ . We note that  $\mu_\psi^h$  is restricted to the interval  $(0, \pi)$ , even though  $\psi_1 \in (0, 2\pi)$ . This is due to the fact that when the EC model (6) is run in two dimensions, as it is here, the responses due to  $\psi_1$  and  $\psi_1 + \pi$  are equivalent. That is, centering the cODF at either  $\mu_\psi$  or  $\mu_\psi + \pi$  produces the same EC response. As such, we only consider values of  $\mu_\psi^h \in (0, \pi)$ , with the understanding that the distribution defined by  $\mu_\psi^h + \pi$  is also a possible solution.

Note that each prior is only meant to avoid redundancy in the solutions. Future work will examine building priors that include information from the materials systems of interest.

**4.3.1. Computation of the MAP estimate.** Using the Bingham distribution, the unknown ODF  $f$  amounts to a set of unknown parameters  $(\nu_1, \nu_2, \dots, \nu_p)$ . In order to compute the MAP estimate of the unknown ODF, we minimize the negative log of the augmented posterior, that is,

$$f_{\text{MAP}} = \arg \min \left\{ -\log(\pi(z|f, \|w_f\|, \bar{w}_f)) + \lambda(-\log(\pi_{\text{prior}}(f))) \right\}, \quad (34)$$

where  $\pi_{\text{prior}}(f)$  is the prior distribution of the Bingham parameters, as detailed in this section. The parameter  $\lambda$  is a regularization parameter; a larger value of  $\lambda$  increases the penalty imposed

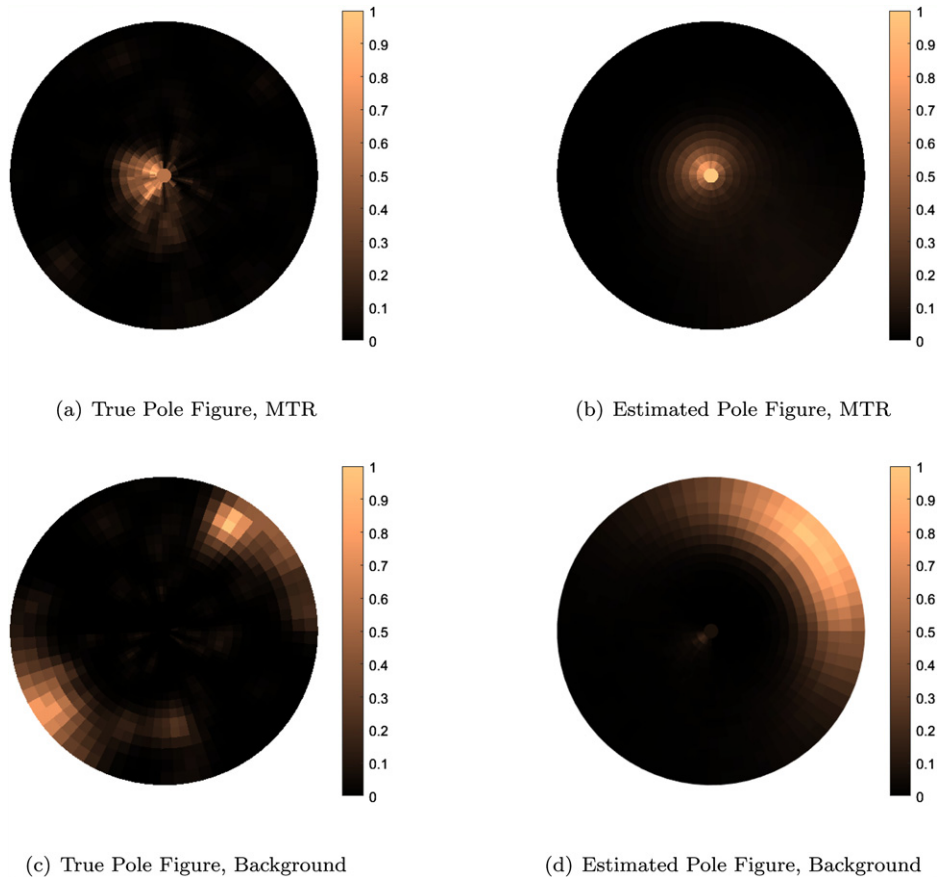


**Figure 8.** True pole figures and pole figures of the MAP estimates for the MTR dataset. Included in this plot are (a)–(b) the results for the MTR and (c)–(d) the results for the background region.

by the prior. We empirically chose a value of  $\lambda = 1 \times 10^4$ . Lower values of  $\lambda$  did not impose a significant penalty when sampling from the augmented posterior.

#### 4.4. Results for dataset 1

The MAP estimates of each of the cODFs are shown plotted in figure 8, along with the pole figures of the true cODFs. The estimated cODFs are, for the most part, in good agreement with the true cODFs. We note that the true pole figure for the background region contains two hot spots; these correspond to two values of the first Euler angle which are separated by  $180^\circ$ . The hot spot in the estimated pole figure matches well to one of the hot spots in the true pole figure. However, the MAP estimate should technically contain a second hot spot, rotated  $180^\circ$  from the first since, as previously mentioned, the EC model yields an equivalent response for the distributions centered at  $\mu_\psi$  and  $\mu_\psi + \pi$ .

We note that neither of the true distributions can be fully described by a single Bingham distribution, but the estimates provides a good approximation of the general shape of the each cODF. In order to better represent the realistic cODFs, we could consider using either a mixture

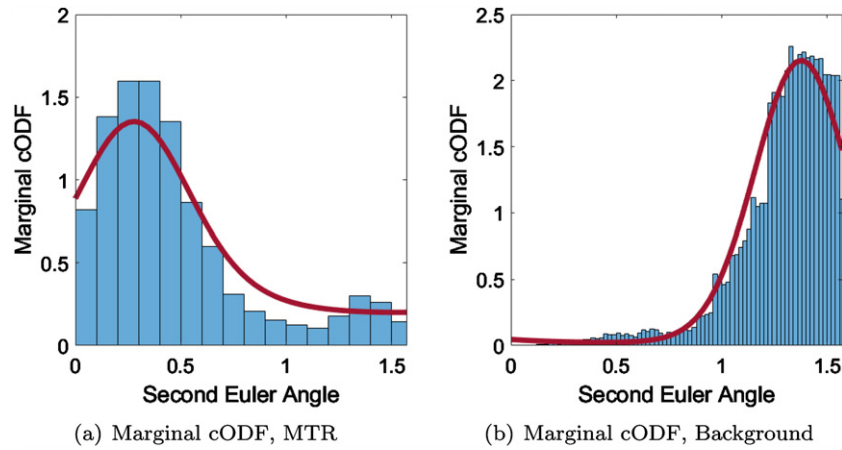


**Figure 9.** Estimated marginal cODF for the (a) MTR and (b) background region. The blue histogram is the true marginal cODF, and the red curve is the MAP estimate.

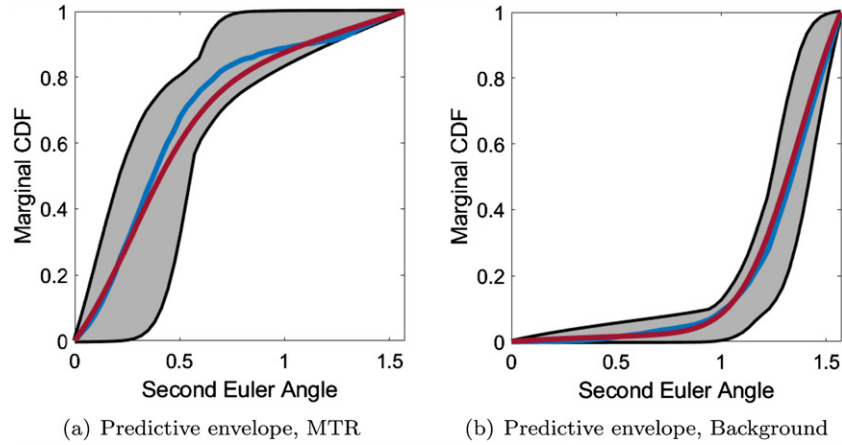


**Figure 10.** Estimated CDF sampling results for the MTR dataset. The 95% predictive envelope is shown in gray. The red line is the MAP estimate of the marginal CDF of the second Euler angle, while the blue curve is the true CDF. Results are shown for both (a) the elliptical MTR region and (b) the background region.

of Bingham distributions, as in [10], or a non-parametric representation, with the trade-off of needing to estimate more parameters in the inverse problem. Finding the best representations for realistic cODFs will likely be the topic of a future work.

Shown in figure 9 are the MAP estimate of the marginal cODF of the second Euler angle, along with the true marginal cODF, computed for both regions. We note that in both cases, the MAP estimate of the marginal cODF matches very well to the true marginal cODF.

We also computed the marginal cumulative distribution function (CDF) of the second Euler angle. This is a way of visualizing the predicted percentage of orientations which fall within a certain range. We repeated this process for both the elliptical MTR region and the background region. Each plot in figure 10 shows the MAP estimate of the marginal CDF of the second

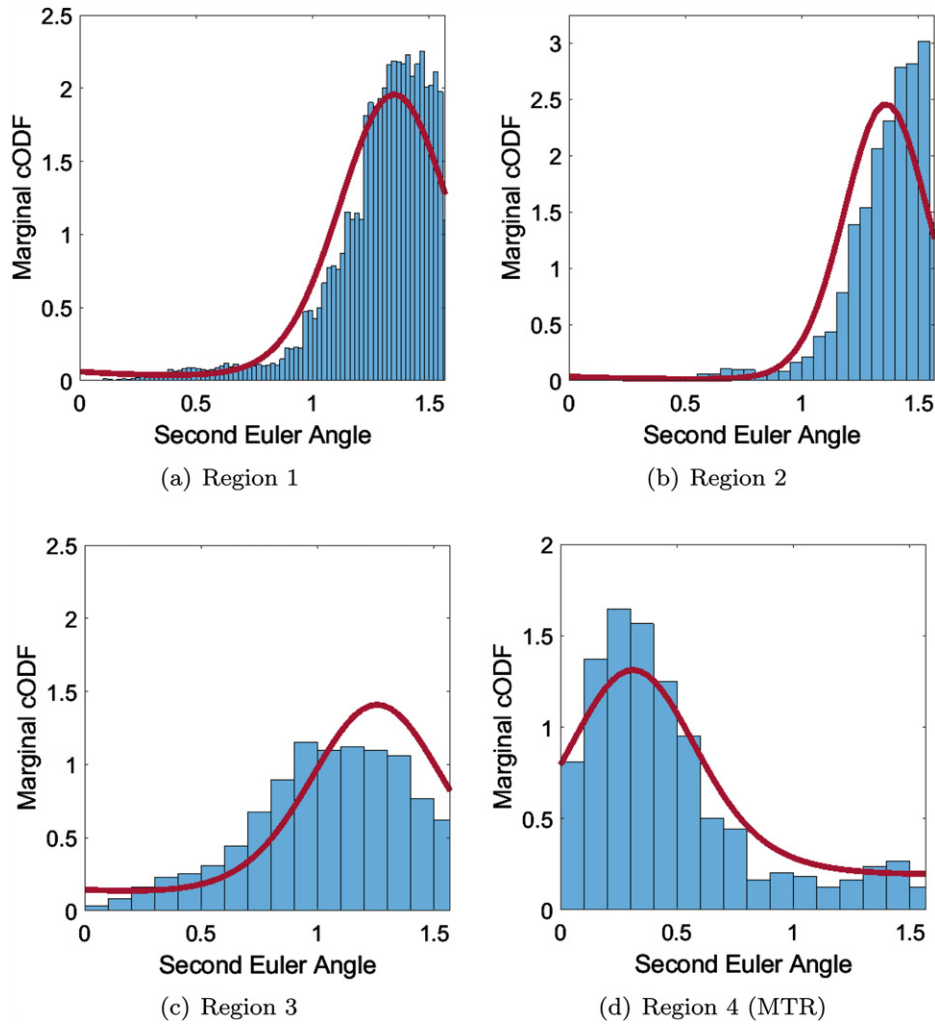


**Figure 11.** Estimated marginal cODFs of the second Euler angle for the four cODFs dataset. The blue histogram is the true marginal cODF, and the red curve is the MAP estimate. The region numbers correspond to the numbers shown in the IPF map in figure 6.

Euler angle, as well as the true marginal CDF. In addition, we generated a sample from the posterior using the delayed rejection adaptive Metropolis (DRAM) algorithm (see [7]). From this sample, we computed the 95% predictive envelope (see, for instance, [3]) of the CDF, shown in gray in figure 10. In both cases, the true CDF lies well within the 95% envelope.

#### 4.5. Results for dataset 2

We drew a sample from the posterior distribution using the DRAM algorithm. The MAP estimate of the marginal cODF of the second Euler angle is shown plotted alongside the true marginal cODF for each region in figure 11. In addition, we computed the marginal CDF of

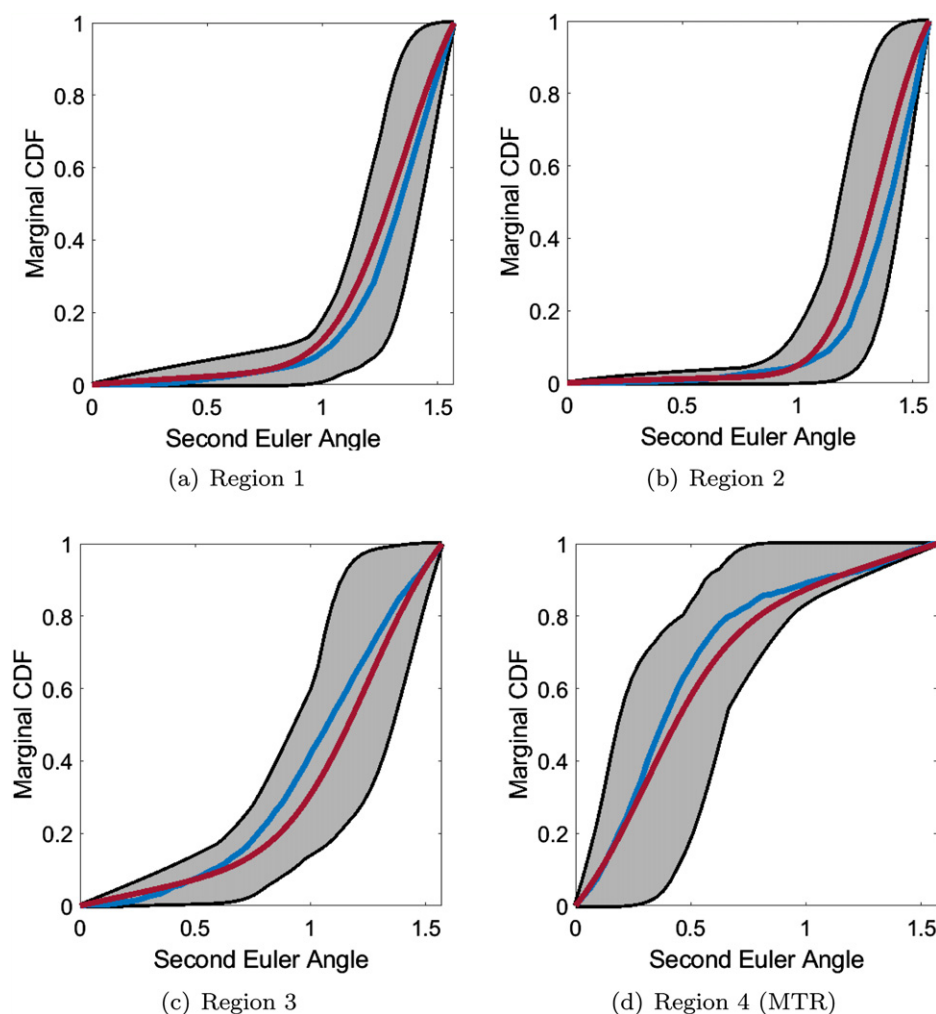


**Figure 12.** Estimated marginal CDFs of the second Euler angle for the four cODFs dataset. The blue curve indicates the true marginal CDF, and the red curve is the MAP estimate. The gray area is the 95% predictive envelope. The region numbers correspond to the numbers shown in the IPF map in figure 6.

the second Euler angle for each region. These results are shown in figure 12. In particular, we show the MAP estimate of the CDF, as well as the 95% predictive envelope.

In all cases, the true CDF lies well within the 95% envelope. It is interesting to note that the MTR in this dataset and the elliptical MTR in the first dataset are governed by the same underlying cODF. However, the 95% predictive envelope on the marginal CDF is noticeably wider for the MTR in the second dataset; recall that this MTR is roughly a quarter of the size of the MTR in the first dataset. Not surprisingly, the size of the MTR seems to have an impact on the ability of the algorithm to confidently estimate its cODF.

## 5. Conclusions

Using the central limit theorem, we have developed a statistical methodology to estimate the individual cODFs that compose a titanium alloy specimen using EC data. This method was successfully demonstrated on two simulated specimens.

While successful, this method does require knowledge of the boundaries between regions that are defined by different cODFs, information that may be nontrivial to obtain. One potential method to determine these boundaries is to use level set inversion on the EC data (see, for instance [8]); this method may have challenges due to the relatively low resolution of EC data. Alternatively, we may consider using a different, high resolution NDE technique altogether to obtain the needed boundaries. This is the topic of future research.

This method also relies on the assumption that the individual grain orientations are independent. While this is true in our simulated specimens, it may not hold for real specimens. The effect of this assumption will be explored when we proceed to using realistic specimens in the inversion; this is a topic for future work. However, we do not believe that this assumption will negatively impact the accuracy of the inversion when using realistic specimens.

In addition, this work used a non-informative prior when solving the inverse problem. There is potential to use the prior to incorporate additional information about the likely shape of the cODFs based on the material of interest. This will also be the topic of future work.

## Acknowledgments

Dr Homa would like to acknowledge support from the Air Force Research Laboratory through contract FA8650-19-F-5230. The authors would like to acknowledge Dr Mike Uchic, Dr Sean Donegan, Dr Adam Pilchak, and Dr Daniel Sparkman for helpful discussions on the materials system of interest. In addition, the authors would also like to acknowledge Dr Amanda Criner for her helpful input on the analysis techniques.

## Data availability statement

The data that support the findings of this study are available upon reasonable request from the authors.

## ORCID iDs

Laura Homa  <https://orcid.org/0000-0003-1913-7691>

## References

- [1] Auld B A and Moulder J C 1999 Review of advances in quantitative eddy current nondestructive evaluation *J. Nondestruct. Eval.* **18** 3–36
- [2] Balanis C A 2012 *Advanced Engineering Electromagnetics* (New York: Wiley)
- [3] Calvetti D and Somersalo E 2008 *Introduction to Bayesian Scientific Computing* (Berlin: Springer)
- [4] Cherry M R, Sathish S, Mooers R D, Pilchak A L and Grandhi R 2017 Modeling of the change of impedance of an eddy current probe due to small changes in host conductivity *IEEE Trans. Magn.* **53** 1–10
- [5] Cherry M, Sathish S, Pilchak A, Cherry A and Blodgett M 2015 Characterization of microstructure with low frequency electromagnetic techniques *AIP Conf. Proc.* **1581** 1456–64

- [6] Del Moral P, Doucet A and Jasra A 2012 An adaptive sequential Monte Carlo method for approximate Bayesian computation *Stat. Comput.* **22** 1009–20
- [7] Haario H, Laine M, Mira A and Saksman E 2006 DRAM: efficient adaptive MCMC *Stat. Comput.* **16** 339–54
- [8] Homa L, Cherry M and Sparkman D 2019 A Bayesian level set method for microtexture region characterization using eddy current data Available online: <https://iastatedigitalpress.com/qnde/article/id/8537/>
- [9] Marjoram P, Molitor J, Plagnol V and Tavaré S 2003 Markov chain Monte Carlo without likelihoods *Proc. Natl Acad. Sci.* **100** 15324–8
- [10] Niezgoda S R and Glover J 2013 Unsupervised learning for efficient texture estimation from limited discrete orientation data *Metall. Mater. Trans. A* **44** 4891–905
- [11] Pilchak A L, Li J and Rokhlin S I 2014 Quantitative comparison of microtexture in near-alpha titanium measured by ultrasonic scattering and electron backscatter diffraction *Metall. Mater. Trans. A* **45** 4679–97
- [12] Pilchak A L, Hutson A, Porter W J, Buchanan D and John R 2016 On the cyclic fatigue and dwell fatigue crack growth response of Ti–6Al–4V *Proc. of the 13th World Conf. on Titanium* (New York: Wiley) 993–8
- [13] Qui J, Ma Y, Lei J, Liu Y, Huang A, Rugg D and Yang R 2014 A comparative study on dwell fatigue of Ti–6Al–2Sn–4Zr–xMo ( $x = 2$  to 6) alloys on a microstructure-normalized basis *Metall. Mater. Trans. A* **45** 6075–87
- [14] Randle V and Engler O 2000 *Introduction to Texture Analysis: Macrotexture, Microtexture, and Orientation Mapping* (London: Gordon and Breach)
- [15] Rowenhorst D, Rollett A D, Rohrer G S, Groeber M, Jackson M, Konijnenberg P J and De Graef M 2015 Consistent representations of and conversions between 3D rotations *Modelling Simul. Mater. Sci. Eng.* **23** 083501
- [16] Sisson S A and Fan Y 2011 Likelihood-free Markov chain Monte Carlo *Handbook of Markov Chain Monte Carlo* ed S Brooks, A Gelman, G L Jones and X Meng (London: Chapman and Hall) pp 313–35
- [17] Sparkman D M 2014 *Spatial Statistical Characterization and Simulation of Microtexture* (San Antonio: The University of Texas)
- [18] Toubal L, Bocher P and Moreau A 2015 Bimodal dwell-fatigue Weibull distribution of forged titanium IMI 834 *Int. J. Damage Mech.* **24** 629–45
- [19] Tucker J C, Groeber M A, Lee Semiatin S and Pilchak A L 2016 Synthetic building and targeted analysis of life-limiting microtextured regions *Proc. 13th World Conf. on Titanium* (New York: Wiley) 1913–8